RSC Advances

PAPER

View Article Online
View Journal | View Issue

Cite this: *RSC Adv.*, 2023, **13**, 30625

Solvent-induced polymorphism in dipodal N-donor ligands containing a biphenyl core†

Simran Chaudhary, Dariusz Kędziera, Zbigniew Rafiński and Liliana Dobrzańska *

Received 21st August 2023
Accepted 6th October 2023

DOI: 10.1039/d3ra05713e

rsc.li/rsc-advances

Polymorph screenings for two related dipodal N-donor ligands containing a biphenyl core, namely 4,4′-bis(pyridin-4-ylmethyl)-1,1′-biphenyl (**1**) and 4,4′-bis(1*H*-imidazol-1-ylmethyl)-1,1′-biphenyl (**2**) were performed, and the new phases were isolated and their crystal structures analysed. Profiling included methods such as PXRD and thermal analysis. Hirshfeld surface analyses, as well as crystal lattice energy calculations provided deeper insight in the interplay of the intermolecular forces and the stability of the isolated phases. Furthermore, our studies revealed the presence of solvent-induced polymorphism, whereby the metastable phase is dominant upon crystallisation from THF (**1a**) and EtOH (**2c**). Upon heating, these phases transform into a more stable form, whereby the transformations were followed by PXRD studies (**1**, **2**).

Introduction

Polymorphism, an intriguing phenomenon concerning the formation of crystal structures[1] that can be defined as the existence of multiple crystalline forms of the same compound,[2] differing by molecular conformation (conformational polymorphs),[3] molecular arrangement (packing polymorphs)[4] or both, has been the subject of intense research in the last few decades. The existence of multiple crystalline forms of the same composition has a big impact, especially on materials science and more specifically within the pharmaceutical industry, as it makes the design of compounds of particular build and properties very challenging.[5] It almost goes without saying that it is crucial to retain the same form of a drug in order not to be surprised by sudden changes in properties caused by the appearance of another form.[6] It is broadly known that various synthetic/crystallisation conditions (solvent effect,[7] the level of supersaturation,[8] temperature[9] and pressure[10]) can lead to the occurrence of polymorphism. The phenomenon is related to the interplay of noncovalent intermolecular forces, for example hydrogen bonds,[11] halogen bonds[12] and π–π interactions,[13] different combinations of which can lead to the formation of disparate crystalline phases. Taking into account the variety of crystal structures of similar lattice energy, which can be formed, it is not trivial to predict the final product of the crystallisation process. This issue is reflected by computational Crystal Structure Prediction methods (CSP) currently being developed, which for a simple organic molecule can generate hundreds of possible polymorphs.[14]

In continuation of our studies encompassing a family of dipodal N-donor ligands,[15] we would like to present the polymorphic behaviour of two related compounds (Scheme 1) namely, 4,4′-bis(pyridin-4-ylmethyl)-1,1′-biphenyl (**1**) and 4,4′-bis(1*H*-imidazol-1-ylmethyl)-1,1′-biphenyl (**2**). Their recrystallization screenings in different solvents allowed us to isolate a series of polymorphs.

Experimental

Reagents and materials

All commercially available chemicals and solvents were of reagent grade and were used without further purification.

Synthetic procedures

Both presented ligands (Scheme 1) were synthesised earlier[16] but the procedures were modified.

Synthesis of 4,4′-bis(pyridin-4-ylmethyl)-1,1′-biphenyl (1). 4,4′-Bis(chloromethyl)biphenyl (2 g, 7.96 mmol), 4-pyridinylboronic acid (2.4 g, 19.52 mmol) and Na_2CO_3 (3.5 g, 32.51 mmol) were weighed and added in a RB flask. Under argon, $Pd(PPh_3)_4$ (0.462 g, 0.4 mmol) was added to the same flask. 1,4-Dioxane (32 ml) and water (16 ml) were added to the above flask,

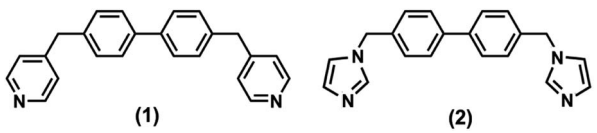

Scheme 1 Representation of the presented N-donor ligands.

Faculty of Chemistry, Nicolaus Copernicus University in Toruń, Gagarina 7, 87-100, Toruń, Poland. E-mail: lianger@umk.pl

† Electronic supplementary information (ESI) available: NMR spectra of **1** and **2**, powder patterns obtained for **1** upon recrystallisation from a range of solvents, packing diagrams of **1a**, **1b**, **2b** and **2c**, thermograms of **1a**, **1b** and **2c**. CCDC 2253373–2253376. For ESI and crystallographic data in CIF or other electronic format see DOI: https://doi.org/10.1039/d3ra05713e

and the reaction mixture was refluxed at 100 °C for 4 h under argon atmosphere. Upon reaction completion (after 4 h, monitored by TLC), the mixture was cooled down, and quenched with water. The aqueous layer was extracted with DCM, and the organic layer was dried over $MgSO_4$ and evaporated under reduced pressure. The resulting solid was purified by flash chromatography (eluent 0 to 3% MeOH in DCM).[17] Yield: 13%.

^{1}H NMR ($CDCl_3$, 700 MHz) δ 8.54 (d, 4H), 7.55 (d, 4H), 7.27 (d, 4H), 7.19 (d, 4H), 4.04 (s, 4H); ^{13}C NMR ($CDCl_3$, 100 MHz) δ 149.9, 139.2, 138.0, 129.5, 127.3, 124.2, 40.9.

Synthesis of 4,4′-bis(1*H*-imidazol-1-ylmethyl)-1,1′-biphenyl (2). A mixture of imidazole (3.36 g, 60 mmol) and KOH (4.08 g, 60 mmol) in 100 ml THF was stirred in a RB flask for 4 h at room temperature. Then, a solution of 4,4′-bis(chloromethyl)biphenyl in 100 ml THF was added dropwise to the above solution. After complete addition, the resulting solution was stirred for 2 days at room temperature, and then the solvent was evaporated. 50 ml of water was added to the obtained yellow solid and the aqueous layer was extracted with DCM. The organic layer was washed with water, dried with $MgSO_4$ and concentrated under reduced pressure. The product was obtained as an off-white solid. Yield: 80%.

^{1}H NMR ($CDCl_3$, 700 MHz) δ 7.65 (s, 2H), δ 7.58 (d, 4H), δ 7.26 (d, 4H), 7.15 (t, 2H), 6.96 (t, 2H), 5.20 (s, 4H); ^{13}C NMR ($CDCl_3$, 100 MHz) δ 140.3, 137.4, 135.6, 129.9, 127.8, 127.6, 119.3, 50.4.

Crystallisation of different forms of 1 and 2

The compounds **1** and **2** were recrystallized from a range of solvents of different geometry and polarity, such as acetone, acetonitrile, DCM, EtOH, MeOH and THF (10 mg of compound/10 ml of solvent). Vials covered with parafilm were left to undergo slow evaporation, which allowed us to obtain good quality crystals in all vials containing **1**. In the case of **2**, crystals suitable for SCXRD studies could only be grown from DCM, MeOH and EtOH (poor quality). The earlier reported crystal structures of **2** (monohydrate **2H** and anhydrous form **2a**) were isolated as unexpected products of the metal complexation reaction by applying slow diffusion of an ethanolic solution of $AgBF_4$ into the ligand solution dissolved in chloroform or by slow diffusion of an aqueous solution of $AgNO_3$ into a solution of ligand dissolved in acetone, respectively.[17]

Measurements

^{1}H and ^{13}C NMR spectra were recorded on Bruker Avance 700 MHz and 400 MHz instruments, respectively and referenced to residual solvent peaks (see Fig. S1 and S2†).

Thermal analyses (TGA, DTA) were performed on a TA Instruments SDT 650 Analyser. All TGA experiments were performed at a heating rate of 2 °C min^{-1} under dry nitrogen with a flow rate of 100 ml min^{-1} covering the temperature range: 25–600 °C.

PXRD patterns were obtained on a Philips X'Pert X-ray diffractometer using CuKα radiation. The voltage and current were 40 kV and 30 mA, respectively. The samples were measured at the 2Θ range of 4–45° with a scan speed of 0.0089° s^{-1}. All data were acquired at ambient temperature. The PXRD data were analysed using Powder Cell[18] and Profex[19] software.

Structure determination

Single-crystal X-ray diffraction data for **1a**, **1b**, **2b** and **2c** were collected on an XtaLAB Synergy-S Dualflex diffractometer equipped with monochromated CuKα radiation ($\lambda = 1.54184$ Å). The crystals were coated with Paratone-N oil and mounted on a loop. Data collection was carried out at 100(2) K to minimize solvent loss, possible structural disorder and thermal motion effects. Data frames were processed (unit cell determination, intensity data integration, correction for Lorentz and polarisation effects, and empirical absorption correction) by using the corresponding diffractometer's software package.[20] The structures were solved by using direct methods with SHELXS-2018/3 (ref. 21) and refined by using full-matrix least-squares methods based on F^2 by using SHELXL-2018/3.[22] The programs Mercury[23] and POV-Ray[24] were both used to prepare molecular graphics. All non-hydrogen atoms were refined anisotropically. All hydrogen atoms were positioned geometrically with C–H = 0.95 Å (aromatic) and 0.99 Å (methylene), and refined as riding, with U_{iso} (H) = 1.2 U_{eq} (C).

A summary of the data collection and structure refinement parameters are provided in Table 1. None of the crystal structures of **1** were reported previously, but as mentioned earlier, two forms of **2** (**2H** and **2a**) were described before.[17] Their unit cell parameters and basic data collection conditions are shown in Table 1. Kitaigorodskii packing indices were calculated by applying the PLATON package.[25] The values shown for **2H** and **2a** are most likely underestimated and can not be directly compared to those of **2b** and **2c**, as the SCXRD data for the former two were collected at room temperature.

Computational methods

Hirshfeld surface analysis. Hirshfeld surface analysis of the polymorphs was carried out using Crystal Explorer 17.[26] 2D fingerprint plots were generated by using a standard 0.6–2.4 Å range including reciprocal contacts.

Crystal lattice energy calculations. The total lattice energy, as well as contributions of its components (coulombic, polarization, dispersion and repulsion), were obtained by applying the program PIXEL.[27] The electron densities in the crystal lattice energies were obtained on MP2/6-31G** level of theory, using the Gaussian09 quantum chemistry package.[28]

Results and discussion

Polymorphs of 4,4′-bis(pyridin-4-ylmethyl)-1,1′-biphenyl (1a/1b)

PXRD screening studies performed for sample **1** recrystallized from a range of solvents indicated the formation of at least two different phases. Especially the powder pattern obtained for crystalline material grown from THF stood out (Fig. S3†), even though there was no striking difference in morphology of the crystals formed in the different solvents. We isolated single-crystals from this solvent, collected SCXRD data, determined

Table 1 Crystal data and details of the refinement parameters for the crystal structures of **1–2**

Compound reference	**1a**	**1b**	**2H**	**2a**	**2b**	**2c**
Chemical formula	$C_{24}H_{20}N_2$	$C_{24}H_{20}N_2$	$C_{20}H_{18}N_4 \cdot H_2O$	$C_{20}H_{18}N_4$	$C_{20}H_{18}N_4$	$C_{20}H_{18}N_4$
Formula mass	336.42	336.42	332.40	314.38	314.38	314.38
a/Å	20.7777(2)	5.76800(5)	4.7126(10)	10.957(1)	5.66180(10)	18.2880(5)
b/Å	10.58810(10)	9.98210(10)	15.269(3)	9.964(1)	14.6008(2)	7.9130(2)
c/Å	8.25020(10)	15.60390(10)	24.148(5)	15.457(2)	19.1251(3)	22.3941(5)
α/°	90	90	90	90	90	90
β/°	94.6050(10)	100.4410(10)	94.024(3)	94.43(1)	90.6510(10)	90
γ/°	90	90	90	90	90	90
Unit cell volume/Å^3	1809.16(3)	883.546(11)	1733.33	1682.4(3)	1580.91(4)	3240.72(14)
Space group	$P2_1/c$	$P2_1$	$P2_1/n$	$P2_1/c$	$P2_1/n$	$Pbca$
No. of formula units per unit cell, Z	4	2			4	8
Temperature/K	100(2)	100(2)	293(2)	293(2)	100(2)	100(2)
Radiation type	CuKα	CuKα	MoKα	MoKα	CuKα	CuKα
Absorption coefficient, μ/mm^{-1}	0.556	0.570			0.633	0.618
No. of reflections measured	39 998	29 193			18 651	27 548
No. of independent reflections	3774	3501			3263	2985
R_{int}	0.0347	0.0238			0.0290	0.0638
Final R_1 values ($I > 2\sigma(I)$)	0.0373	0.0256			0.0342	0.0382
Final w$R(F^2)$ values ($I > 2\sigma(I)$)	0.0936	0.0674			0.0863	0.0921
Final R_1 values (all data)	0.0440	0.0260			0.0384	0.0520
Final w$R(F^2)$ values (all data)	0.0978	0.0677			0.0892	0.0989
Goodness of fit on F^2	1.028	1.038			1.052	1.033
Flack parameter		−0.13(10)				
Kitaigorodskii packing indices	68.4	70.3	68.2	66.4/66.3	71.6	69.7

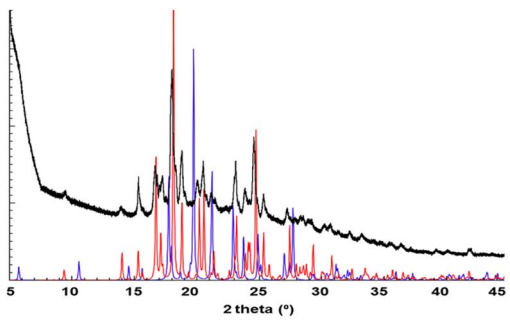

Fig. 1 Overlay of the simulated PXRD patterns generated from crystal structures recrystallized from THF (red, **1a**) and MeOH (blue, **1b**), and experimental PXRD pattern obtained for the sample after recrystallization from THF (black).

the crystal structure (**1a**) and generated its powder pattern, which corresponded very well with the experimentally determined trace (Fig. 1). Furthermore, a good quality single crystal was isolated from MeOH and the crystal structure was determined (**1b**). Powder Cell indicated the absence of **1a** in the solid recrystallized from MeOH. Moreover, the phase **1b** shows its dominance in all studied solids, apart from the one obtained from THF, in which its contribution is negligible, at *ca.* 2%. Interestingly increasing the concentration of the solute in THF (15 or 20 mg/10 ml) leads to the formation of **1b** exclusively.

The isolated polymorphs **1a** and **1b** crystallise in monoclinic systems of the $P2_1/c$ and $P2_1$ space groups, respectively. It is worth mentioning that pairs of polymorphs crystallising in a combination of centrosymmetric and acentric space groups have previously received quite some attention, as studying these could facilitate gaining control over the formation of acentric packings.[29] The molecules in these two crystalline forms adopt different conformations as shown in Fig. 2. The dihedral angles between the planes of the benzene rings are 34° and 35° for **1a** and **1b**, respectively, *versus* 57° and 20° between the planes of the pyridine rings.

The molecular packing in both crystalline phases involves sets of different intermolecular forces even though their choices in the case of this compound are rather limited (Fig. S4†). As could be expected, a large contribution is coming from C–H···N interactions leading to the formation of 3D supramolecular assemblies. These are further supported by C–H···π forces (Table 2), involving methylene groups and pyridine rings as donors and benzene rings as acceptors (**1a**), whereas for **1b** either pyridine rings act as donors and pyridine rings as

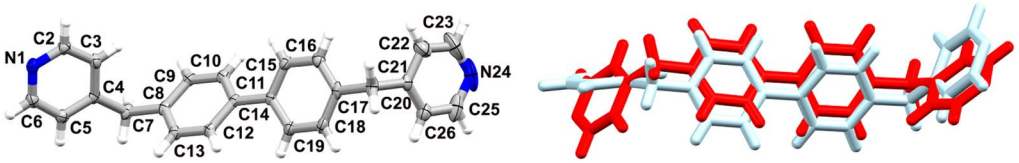

Fig. 2 On the left: molecular structure of **1a** with atomic displacement plot shown at 50% probability; the labelling refers also to **1b**, on the right: overlay of **1a** (red) and **1b** (blue); RMSD 1.0522 Å.

Table 2 Hydrogen bonding parameters for **1a** and **1b**[a]

Compound	D–H···A	H···A (Å)	D···A (Å)	D–H···A (°)
1a	C5–H5···N1^{i}	2.61	3.553(2)	174
	C13–H13···N1^{i}	2.56	3.485(2)	163
	C10–H10···N24^{ii}	2.86	3.626(2)	139
	C16–H16···N24^{iii}	2.74	3.617(2)	153
	C20–H20A···N24^{iv}	2.70	3.474(2)	135
	C25–H25···N24^{v}	2.94	3.790(2)	150
	C7–H7A···Cg$_1$^{vi}	2.85	3.767(1)	154
	C23–H23···Cg$_1$^{ii}	2.95	3.829(1)	155
1b	C7–H7B···N1^{i}	2.73	3.521(2)	137
	C13–H13···N1^{i}	2.74	3.585(2)	149
	C22–H22···N1^{ii}	2.73	3.507(2)	140
	C5–H5···N24^{iii}	2.68	3.381(2)	131
	C16–H16···Cg$_1$^{iv}	2.78	3.683(2)	158
	C2–H2···Cg$_2$^{v}	2.90	3.572(2)	129
	C23–H23···Cg$_2$^{vi}	2.89	3.680(2)	141
	C25–H25···Cg$_1$^{vii}	2.95	3.697(2)	136

[a] (**1a**) Cg$_1$ is the centroid of benzene ring C14–C19; (**1b**) Cg$_1$ is the centroid of benzene ring C8–C13, Cg$_2$ is the centroid of pyridine ring N1–C6, symmetry codes (**1a**): (i) $-x$,1/2 + y,$-$1/2 $-$ z, (ii) 1 $-$ x,1 $-$ y,1 $-$ z, (iii) 1 $-$ x,1/2 + y,1/2 $-$ z, (iv) 1 $-$ x,1 $-$ y,$-z$, (v) x,1/2 $-$ y,$-$1/2 + z, (vi) x, y, $-$1 + z; (**1b**): (i) $-x$ + 1,y $-$ 1/2,$-z$ + 1, (ii) x,y,z + 1, (iii) $-x$,y + 1/2,$-z$ + 2, (iv) 1 $-$ x, 1/2 + y,2 $-$ z, (v) 1 + x,y,$-$1 + z, (vi) 1 $-$ x,$-$1/2 + y,2 $-$ z, (vii) $-x$,$-$1/2 + y,2 $-$ z.

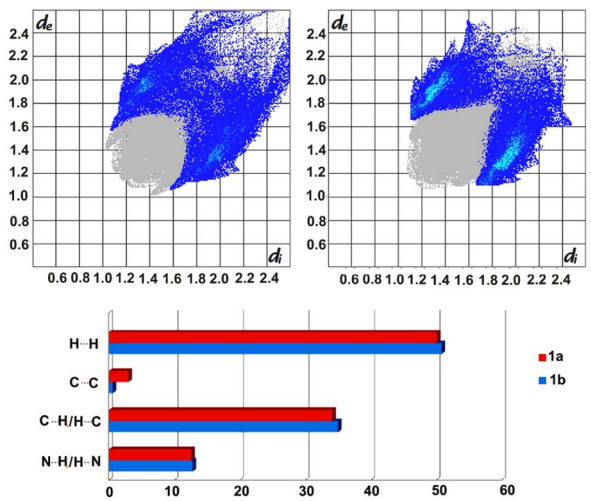

Fig. 3 Fingerprint plots (top) for form **1a** (left) and **1b** (right) with the contribution of C···H/H···C contacts indicated in blue. Bottom: estimated contributions (percentages) of selected intermolecular forces stabilizing the formation of **1a** and **1b**.

acceptors or benzene and pyridine rings as donors and benzene rings as acceptors. Furthermore, weak intermolecular π–π interactions between two adjacent pyridine rings containing N24 (symmetry operator: 1 $-$ x, 1 $-$ y, $-z$) are present in **1a**, with a centroid–centroid distance of 3.7092(6) Å. The most striking differences between these two crystal structures lie in the strength of the interactions formed, the involvement of different molecular units in their formation, and the presence or absence of π–π interactions.

Further analyses of the intermolecular forces stabilising the crystal structures, by applying Crystal Explorer, allowed to visualise these in the form of fingerprint plots, as well as to estimate their percentage contributions, which indicate, among others, the presence of stronger C–H···π interactions in **1b** (Fig. 3), as observed earlier.

Moreover, the calculated enrichment ratios[30] show once again the importance of C–H···N and C–H···π interactions in stabilising the crystal packing in **1a** and **1b**, with slightly higher dominance of the former in **1a** (1.33 *versus* 1.15) and the latter in **1b** (1.27 *vs.* 1.20).

The crystal lattice energy calculations (Table 3) indicate a lower stability of form **1a**, which is in good agreement with the

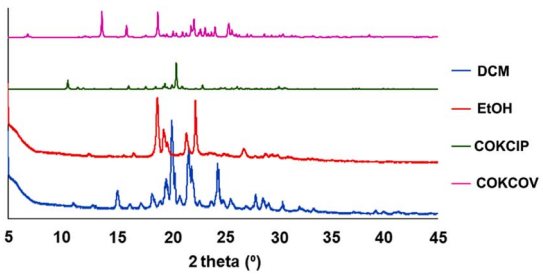

Fig. 4 PXRD patterns obtained for samples of **2** after recrystallization from DCM (blue) and EtOH (red) and simulated PXRD patterns generated from crystal structures of **2H** (COKCOV, pink) and **2a** (COKCIP, green).

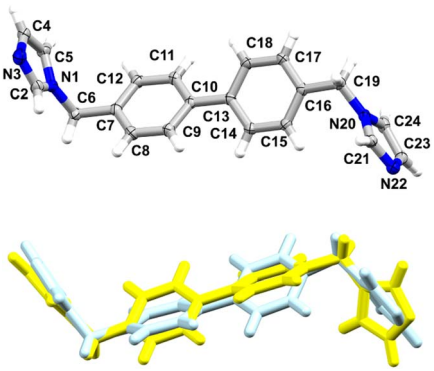

Fig. 5 Overlay of **2b** (blue) and **2c** (yellow) indicating the difference in position of one of the imidazole rings (RMS deviation is 0.9791 Å).

Table 3 Interaction energies calculated by the program PIXEL for the two forms of **1** (kJ mol^{-1} units)

Energy component/form	Coulombic	Polarisation	Dispersion	Repulsion	Energy in total
1a	−51.0	−22.9	−198.3	94.9	−177.4
1b	−50.8	−21.9	−208.8	96.7	−184.9

lower Kitaigorodskii packing index (see KI indices in Table 1). The results show once again a similar input of different forces, with the major difference in input of the dispersion term, which delivers the major contribution to stabilizing both crystalline phases.

Table 4 Hydrogen bonding parameters for **2a–2c**[a]

Compound	D–H···A	H···A (Å)	D···A (Å)	D–H···A (°)
2a1	C6–H3···N3^{i}	2.94	3.820	158
	C10–H8···N3^{i}	2.96	3.798	150
	C18–H15···N3^{ii}	2.93	3.792	155
	C3–H1···N5^{iii}	2.90	3.752	153
	C8–H5···N5^{iv}	2.67	3.524	154
	C13–H11···N5^{v}	2.76	3.675	168
	C4–H2···Cg$_1$^{vi}	2.69	3.575	159
	C10–H8···Cg$_2$^{vii}	2.73	3.565	150
	C12–H10···Cg$_3$^{viii}	2.95	3.677	136
2a2	C9–H6···N4^{i}	2.95	3.598	128
	C10–H8···N4^{ii}	2.933	3.853	173
	C3–H1···N5^{iii}	2.90	3.752	153
	C8–H5···N5^{iv}	2.67	3.524	154
	C13–H11···N5^{v}	2.76	3.675	169
	C4–H2···Cg$_1$^{vi}	2.69	3.5751	159
	C10–H8···Cg$_2$^{i}	2.73	3.5650	150
	C12–H10···Cg$_3$^{iii}	2.95	3.6773	136
2b	C17–H17···N3^{i}	2.851	3.264(2)	107
	C18–H18···N3^{ii}	2.933	3.681(2)	137
	C19–H19B···N3^{i}	2.733	3.318(2)	118
	C19–H19A···N3^{iii}	2.57	3.537(2)	164
	C8–H8···N22^{iv}	2.687	3.589(2)	154
	C6–H6B···N22^{iv}	2.833	3.708(2)	159
	C5–H5···Cg$_1$^{v}	2.70	3.385(1)	129
	C14–H14···Cg$_2$^{vi}	2.94	3.656(1)	133
	C18–H18···Cg$_3$^{ii}	2.90	3.714(1)	144
	C21–H21···Cg$_4$^{vii}	2.90	3.835(1)	167
2c	C19–H19B···N3^{i}	2.702	3.572(2)	147
	C21–H21···N3^{ii}	2.852	3.629(2)	140
	C2–H2···N22^{iii}	2.825	3.577(2)	137
	C6–H6A···N22^{iii}	2.494	3.399(2)	152
	C6–H6B···N22^{iv}	2.809	3.677(2)	147
	C12–H12···N22^{iv}	2.960	3.642(2)	130
	C12–H12···Cg$_1$^{iv}	2.78	3.551(1)	139
	C19–H19A···Cg$_2$^{vi}	2.83	3.811(1)	169
	C23–H23···Cg$_2$^{vii}	2.82	3.761(1)	173

[a] (**2a1**) Cg$_1$ is the centroid of the benzene ring containing C5, Cg$_2$ is the centroid of the imidazole ring containing N1, Cg$_3$ is the centroid of the imidazole ring containing N2; (**2a2**) Cg$_1$ is the centroid of the benzene ring containing C5, Cg$_2$ is the centroid of the imidazole ring containing N1, Cg$_3$ is the centroid of the imidazole ring containing N2; (**2b**) Cg$_1$ is the centroid of imidazole ring N20–C24, Cg$_2$ is the centroid of benzene ring C7–C12, Cg$_3$ is the centroid of imidazole ring N1–C5, Cg$_4$ is the centroid of benzene ring C13–C18; (**2c**) Cg$_1$ is the centroid of imidazole ring N20–C24, Cg$_2$ is the centroid of benzene ring C13–C18, symmetry codes (**2a1**): (i) $1-x,-1/2+y,1/2-z$, (ii) $1-x,1/2+y,1/2-z$, (iii) $2-x,-1/2+y,-1/2-z$, (iv) $-x+2,-x,-y$ (v) $2-x,1/2+y,-1/2-z$, (vi) $1-x,-y,-z$ (vii) $1-x,-1/2+y,1/2-z$, (viii) $2-x,1/2+y,-1/2-z$; (**2a2**): (i) $1-x,1/2+y,1/2-z$, (ii) $1-x,-1/2+y,1/2-z$, (iii) $2-x,-1/2+y,-1/2-z$, (iv) $2-x,-y,-z$, (v) $2-x,1/2+y,-z-1/2$, (vi) $1-x,-y,-z$, (vii) $-x,-1/2+y,1/2-z$; (**2b**): (i) $1/2-x,1/2+y,1/2-z$, (ii) $3/2-X,1/2+Y,1/2-Z$, (iii) $-1/2+x,1/2+y,1/2-z$, (iv) $-x,-y,1-z$, (v) $3/2+X,1/2-Y,-1/2+Z$, (vi) $1-X,-Y,1-Z$, (vii) $-1+x,y,z$; (**2c**): (i) $x,1/2-y,1/2+z$, (ii) $3/2-x,1-y,1/2+z$, (iii) $x,3/2-y,-1/2+z$, (iv) $2-x,1-y,1-z$, (vi) $3/2-x,1/2+y,z$, (vii) $2-x,2-y,1-z$.

To analyse the system further, thermal analyses (TG/DTA) of **1a** and **1b** were performed (Fig. S5 and S6†), which indicated a phase transition taking place in the case of **1a** at *ca.* 100 °C. This was confirmed by a PXRD study, as heating a sample of **1a** at 110 °C for 2 min revealed that this leads to irreversible conversion to **1b**.

Polymorphs of 4,4′-bis(1*H*-imidazol-1-ylmethyl)-1,1′-biphenyl (2a/2b/2c)

The crystal structure of **2** was reported and deposited at CSD earlier (refcode: COKCIP, **2a**) as well as its corresponding monohydrated form (refcode: COKCOV, **2H**). PXRD screening of solids grown from a range of solvents revealed the formation of at least two additional phases (Fig. 4). In DCM and THF, the form **2b** was present exclusively, as shown by PXRD and by applying Powder Cell. Solvents such as MeOH, acetone and acetonitrile led to the formation of mixtures of **2H** and **2b** with a contribution of more than 70% of the latter (the highest contribution of **2b** was noticed in acetone, at 92%). Interestingly, the powder pattern of crystalline material grown from EtOH allowed for isolation of another phase (**2c**, with a contribution of *ca.* 74%), which forms a mixture with **2H** (**2b** was absent in this case).

Though the crystals of **2c** were of poor quality, we managed to select a crystal suitable for SCXRD measurements (Fig. 5).

2a and **2b** crystallise in monoclinic systems of the $P2_1/c$ and $P2_1/n$ space groups respectively, whereas **2c** crystallises in the space group *Pbca* of a higher symmetry orthorhombic system. As reported earlier, one of the imidazole rings in **2a** shows positional N/C disorder (50 : 50), rendering a very accurate comparison of **2a** with the other two phases impossible. Comparing the conformation adopted by the ligand in **2b** with the orientations adopted by the two components **2a1** and **2a2** (disorder), indicated certain differences, especially in the position of one of the imidazole rings (Fig. S7,† RMS deviation of 1.1590 Å for **2a1** and RMS deviation of 0.8922 Å for **2a2**).

Another orientation of the imidazole ring is present in **2c** which is facilitated by the flexibility of the molecule. The torsion angles C7–C6–N1–C2 and C16–C19–N20–C21, corresponding with the labelling in Fig. 4, are as follows: 89°/102°, 87°/−99°, 92°/−148° for **2a**, **2b** and **2c** respectively.

The dihedral angles between the planes of the benzene rings are 33°, 31°, 34° for **2a**, **2b** and **2c** respectively, *versus* 10°, 11°

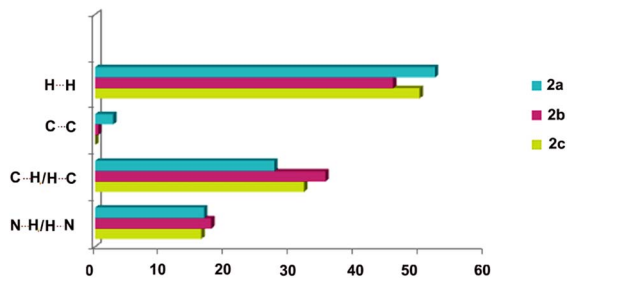

Fig. 6 Estimated contributions (percentages) of selected intermolecular contacts to the Hirshfeld surface in **2a** (blue), **2b** (purple) and **2c** (green).

Table 5 Interaction energies calculated by the program PIXEL for the polymorphs of 2 (kJ mol^{-1} units)

Energy component/Form	Coulombic	Polarisation	Dispersion	Repulsion	Energy in total
2a1	−43.3	−23.6	−172.1	69.3	−169.7
2a2	−56.5	−27.1	−174.2	82.5	−175.2
2a(av)[a]	−49.9	−25.35	−173.15	75.9	−172.5
2b	−72.7	−31.1	−202.8	103.9	−202.7
2c	−74.8	−29.6	−196.1	100.2	−200.3

[a] As this is an average of **2a** disordered components, the values are (very) rough estimates.

and 61° between the corresponding planes of the imidazole rings. Like in **1**, the molecular packing in **2a–2c** involves weak C–H···N hydrogen bonds, leading to the formation of 3D supramolecular assemblies supported by C–H···π interactions (Table 4, Fig. S8†). π–π interactions are absent in this series.

It is worth mentioning that estimating the contributions of the different intermolecular contacts in the two separated forms of **2a**, namely **2a1** and **2a2** contributing equally to molecular disorder, by applying Crystal Explorer, indicated the interplay between H···N (16 : 17.9%) and H···H (52.6 : 51.4%) forces. The results were further averaged and compared with **2b** and **2c** as presented in Fig. 6, indicating the largest contribution of hydrogen bonds in the case of **2b** which, as shown below, is the most energetically favoured phase.

The crystal lattice energy calculation (Table 5) indicated the higher stability of form **2b** over **2c**, which is in good agreement with the higher Kitaigorodskii packing index of **2b** (see KI indices in Table 1). It also pointed out a lower stability of phase **2a**, the presence of which was not observed in any of the studied solids, and which was previously isolated in solid form after silver salt complexation. However the results for this particular phase are not very accurate, as the data set was collected at room temperature and additionally the molecule shows disorder. The lowest input of coulombic/polarisation factors observed for **2a** could be the consequence of a lower input of C–H···π interactions, as shown on the histogram presented in Fig. 6. The results once again reveal that the dispersion term delivers the major contribution to stabilizing these three crystal phases.

To analyse the system further, thermal analyses (TG/DTA) of the solids obtained from DCM and EtOH were performed. These indicated a phase transition taking place at *ca*. 140 °C in the case of solid grown from EtOH (Fig. S9†). A PXRD study revealed that after heating this sample at 150 °C for 3 min, the monohydrate is completely converted to **2b**, whereas the **2c** phase is only partially converted. Upon extended heating at this temperature or after time (3 days in air), **2c** is completely converted to **2b**. Interestingly, comparing the molecular packings formed by monohydrated **2H** and **2b** indicates the presence of the same main packing features, which could facilitate the dehydration/hydration process. Furthermore, the results of thermal analyses pointed out much higher thermal stability of the imidazole based compounds (**2**) (*ca.* 30 °C) over the pyridine analogues (**1**).

Conclusions

Polymorph screenings performed in a series of solvents of different geometry and polarity, such as acetone, acetonitrile, DCM, EtOH, MeOH and THF on two compounds (**1** and **2**) containing a biphenyl core allowed us to reveal two new phases for each.

The ability to form polymorphs is, among others, the result of the conformational flexibility of these molecules, containing aromatic rings which can rotate freely. In both cases one or more solvents could be identified, leading exclusively to the formation of the energetically more stable phase, such as MeOH in the case of **1** and DCM and THF in the case of **2**. Moreover, we could also pinpoint solvents in which the metastable form was predominantly present, namely THF and EtOH, respectively, and follow the irreversible transformations of the isolated metastable forms to the stable arrangement upon heating. The presented observations show that, even in the case of similarly built compounds with a composition limiting the formation of intermolecular interactions through lack of strong hydrogen bond donors, the solvent effect on the crystallisation process can tremendously differ. Furthermore, not only the transformation of a metastable to a stable phase of different molecular packing was observed, but also the dehydration of monohydrate **2**, transforming to the energetically favoured phase **2b** of similar packing. Studies on related systems, as well as investigations of the solvent effect on the nucleation/crystallisation process supported by computational methods, are ongoing.

Conflicts of interest

There are no conflicts to declare.

Acknowledgements

LD and SC would like to thank the National Science Centre – Poland for grant no. 2014/14/E/ST5/00611 and the University Centre of Excellence "Astrophysics and Astrochemistry". LD, ZR and SC would also like to thank the programme Excellence Initiative – Research University for funding the research group of Crystal Engineering and Advanced Solid-State Characterisation.

References

1 A. J. Cruz-Cabeza, N. Feeder and R. J. Davey, *Commun. Chem.*, 2020, **3**, 142.

2 (*a*) J. Bernstein, *Polymorphism in Molecular Crystals*, Oxford University Press, New York, 2002; (*b*) J. P. Brog, C. L. Chanez, A. Crochet and K. M. Fromm, *RSC Adv.*, 2013, **3**, 16905–16931.

3 (*a*) A. Nangia, *Acc. Chem. Res.*, 2008, **41**, 595–604; (*b*) A. J. Cruz-Cabeza and J. Bernstein, *Chem. Rev.*, 2014, **114**, 2170–2191; (*c*) J. Bernstein and A. T. Hagler, *J. Am. Chem. Soc.*, 1978, **100**, 673–681.

4 A. J. Cruz-Cabeza, S. M. Reutzel-Edens and J. Bernstein, *Chem. Soc. Rev.*, 2015, **44**, 8619–8635.

5 (*a*) M. T. Ruggiero, J. Axel Zeitler and T. M. Korter, *Phys. Chem. Chem. Phys.*, 2017, **19**, 28502–28506; (*b*) M. Wehner, M. I. S. Röhr, M. Bühler, V. Stepanenko, W. Wagner and F. Würthner, *J. Am. Chem. Soc.*, 2019, **141**, 6092–6107; (*c*) A. Langenstroer, K. K. Kartha, Y. Dorca, J. Droste, V. Stepanenko, R. Q. Albuquerque, M. R. Hansen, L. Sánchez and G. Fernández, *J. Am. Chem. Soc.*, 2019, **141**, 5192–5200.

6 R. Hilfiker and M. V. Raumer, *Polymorphism in the Pharmaceuticals Industry*, Wiley-VCH Verlag GmbH & Co. KGaA, 2018, pp. 1–30.

7 (*a*) P. Shi, S. Xu, S. Du, S. Rohani, S. Liu, W. Tang, L. Jia, J. Wang and J. Gong, *Cryst. Growth Des.*, 2018, **18**, 5947–5956; (*b*) O. Ochs, M. Hocke, M. Hocke, S. Spitzer, S. Spitzer, W. M. Heckl, W. M. Heckl, N. Martsinovich, M. Lackinger and M. Lackinger, *Chem. Mater.*, 2020, **32**, 5057–5065; (*c*) S. Long, P. Zhou, S. Parkin and T. Li, *CrystEngComm*, 2015, **17**, 2389–2397; (*d*) R. Soto, V. Verma and C. Rasmuson, *Cryst. Growth Des.*, 2020, **20**, 1985–1996; (*e*) K. Dyk, V. Kinzhybalo, G. Czernel, W. Grudziński, Y. Horak, S. Butenko and D. M. Kamiński, *CrystEngComm*, 2023, **25**, 971–980.

8 (*a*) J. Ouyang, J. Chen, I. Rosbottom, W. Chen, M. Guo and J. Y. Y. Heng, *CrystEngComm*, 2021, **23**, 813–823; (*b*) T. Zhang, Y. Liu, S. Du, S. Wu, D. Han, S. Liu and J. Gong, *Cryst. Growth Des.*, 2017, **17**, 6123–6131; (*c*) S. Supriya, S. Sivan and K. Srinivasan, *Cryst. Res. Technol.*, 2018, **53**, 1700239.

9 (*a*) Y. Liu, L. Jia, S. Wu, S. Xu, X. Zhang, S. Jiang and J. Gong, *CrystEngComm*, 2019, **21**, 2790–2798; (*b*) V. K. Srirambhatla, R. Guo, D. M. Dawson, S. L. Price and A. J. Florence, *Cryst. Growth Des.*, 2020, **20**, 1800–1810; (*c*) T. N. Drebushchak, V. A. Drebushchak, N. A. Pankrushina and E. V. Boldyreva, *CrystEngComm*, 2016, **18**, 5736–5743; (*d*) X. Liu, A. S. Gibbs, G. S. Nichol, C. C. Tang, K. S. Knight, P. J. Dowding, I. More and C. R. Pulham, *CrystEngComm*, 2018, **20**, 6885–6893.

10 (*a*) F. Safari, A. Olejniczak and A. Katrusiak, *Cryst. Growth Des.*, 2019, **19**, 5629–5635; (*b*) T. Yan, Y. Deng, Z. Yu, E. John, R. Han, Y. Yao and Y. Liu, *J. Phys. Chem. C*, 2021, **125**, 8582–8588.

11 (*a*) T. Aizawa, K. Aratsu, S. Datta, T. Mashimo, T. Seki, T. Kajitani, F. Silly and S. Yagai, *Chem. Commun.*, 2020, **56**, 4280–4283; (*b*) I. C. B. Martins, J. R. B. Gomes, M. T. Duarte and L. Mafra, *Cryst. Growth Des.*, 2017, **17**, 428–432.

12 (*a*) P. Pang, Y. Wang, X. Miao, B. Li and W. Deng, *New J. Chem.*, 2021, **45**, 6811; (*b*) H. R. Khavasi and A. A. Tehrani, *CrystEngComm*, 2013, **15**, 5813–5820; (*c*) K. Raatikainen and K. Rissanen, *CrystEngComm*, 2009, **11**, 750–752.

13 (*a*) Z. Xie, L. Liu, B. Yang, G. Yang, L. Ye, M. Li and Y. Ma, *Cryst. Growth Des.*, 2005, **5**, 1959–1964; (*b*) M. A. P. Martins, M. Hörner, J. Beck, A. Z. Tier, A. L. Belladona, A. R. Meyer, N. Zanatta, H. G. Bonacorso and C. P. Frizzo, *CrystEngComm*, 2016, **18**, 3866–3876.

14 (*a*) R. M. Bhardwaj, J. A. McMahon, J. Nyman, L. S. Price, S. Konar, I. D. H. Oswald, C. R. Pulham, S. L. Price and S. M. Reutzel-Edens, *J. Am. Chem. Soc.*, 2019, **141**, 13887–13897; (*b*) C. Greenwell and G. J. O. Beran, *Cryst. Growth Des.*, 2020, **20**, 4875–4881; (*c*) M. Vasileiadis, C. C. Pantelides and C. S. Adjiman, *Chem. Eng. Sci.*, 2015, **121**, 60–76; (*d*) X. Li, X. Ou, B. Wang, H. Rong, B. Wang, C. Chang, B. Shi, L. Yu and M. Lu, *Commun. Chem.*, 2020, **3**, 152.

15 (*a*) S. Chaudhary, D. Kędziera and L. Dobrzańska, *Polyhedron*, 2022, **224**, 115989; (*b*) L. Dobrzańska, *Materials*, 2022, **15**, 1852; (*c*) M. Arhangelskis, L. Van Meervelt and L. Dobrzańska, *CrystEngComm*, 2021, **23**, 317–323; (*d*) J. Alen, L. Van Meervelt, W. Dehaen and L. Dobrzańska, *CrystEngComm*, 2015, **17**, 8957–8964.

16 (*a*) M. Fujita, M. Aoyagi, F. Ibukuro, K. Ogura and K. Yamaguchi, *J. Am. Chem. Soc.*, 1998, **120**, 611–612; (*b*) P. K. Dhal and F. H. Arnold, *Macromolecules*, 1992, **25**, 7051–7059.

17 L. Carlucci, G. Ciani, S. Maggini and D. M. Proserpio, *CrystEngComm*, 2008, **10**, 1191–1203.

18 W. Kraus and G. Nolze, *J. Appl. Crystallogr.*, 1996, **29**, 301–303.

19 N. Döeblin and R. Kleeberg, *J. Appl. Crystallogr.*, 2015, **48**, 1573–1580.

20 Rigaku Oxford Diffraction, *CrysAlisPro Software System, version 1.171.38.41*, Rigaku Corporation, Oxford, UK, 2015.

21 G. M. Sheldrick, *Acta Crystallogr.*, 2008, **A64**, 112–122.

22 G. M. Sheldrick, *Acta Crystallogr.*, 2015, **C71**, 3–8.

23 C. F. Macrae, I. J. Bruno, J. A. Chisholm, P. R. Edgington, P. McCabe, E. Pidcock, L. Rodriguez-Monge, R. Taylor, J. Van De Streek and P. A. Wood, *J. Appl. Crystallogr.*, 2008, **41**, 466–470.

24 **http://www.povray.org/**.

25 A. L. Spek, *Platon*, Utrecht University, Utrecht, The Netherlands, 1980–2021.

26 P. R. Spackman, M. J. Turner, J. J. McKinnon, S. K. Wolff, D. J. Grimwood, D. Jayatilaka and M. A. Spackman, *J. Appl. Crystallogr.*, 2021, **54**, 1006–1011.

27 (*a*) A. Gavezzotti, *J. Phys. Chem.*, 2003, **B107**, 2344–2353; (*b*) A. Gavezzotti, *Mol. Phys.*, 2008, **106**, 1473–1485.

28 M. J. Frisch, G. W. Trucks, H. B. Schlegel, G. E. Scuseria, M. A. Robb, J. R. Cheeseman, G. Scalmani, V. Barone, B. Mennucci, G. A. Petersson, H. Nakatsuji, M. Caricato, X. Li, H. P. Hratchian, A. F. Izmaylov, J. Bloino, G. Zheng, J. L. Sonnenberg, M. Hada, M. Ehara, K. Toyota, R. Fukuda, J. Hasegawa, M. Ishida, T. Nakajima, Y. Honda, O. Kitao, H. Nakai, T. Vreven, J. A. Montgomery Jr,

J. E. Peralta, F. Ogliaro, M. Bearpark, J. J. Heyd, E. Brothers, K. N. Kudin, V. N. Staroverov, T. Keith, R. Kobayashi, J. Normand, K. Raghavachari, A. Rendell, J. C. Burant, S. S. Iyengar, J. Tomasi, M. Cossi, N. Rega, J. M. Millam, M. Klene, J. E. Knox, J. B. Cross, V. Bakken, C. Adamo, J. Jaramillo, R. Gomperts, R. E. Stratmann, O. Yazyev, A. J. Austin, R. Cammi, C. Pomelli, J. W. Ochterski, R. L. Martin, K. Morokuma, V. G. Zakrzewski, G. A. Voth, P. Salvador, J. J. Dannenberg, S. Dapprich, A. D. Daniels, O. Farkas, J. B. Foresman, J. V. Ortiz, J. Cioslowski, and D. J. Fox, *Gaussian 09, Revision D.01*, Gaussian, Inc., Wallingford CT, 2013.

29 L. N. Kuleshova, D. W. M. Hofmann and M. Y. Antipin, *Crystallogr. Rep.*, 2005, **50**, 167–176.

30 C. Jelsch, K. Ejsmont and L. Huder, *IUCrJ*, 2014, **1**, 119–128.